Engineering Fracture Mechanics 269 (2022) 108555

Contents lists available at ScienceDirect

Engineering Fracture Mechanics

journal homepage: www.elsevier.com/locate/engfracmech

The double cantilever beam test applied to mode I fracture characterization of polyamide 12 processed by selective laser sintering technology

A.C. Lopes [a,b,*], E.C. Silva [a,b], N. Dourado [c], M.F.S.F. de Moura [d], A.M. Sampaio [a,b,e], A.J. Pontes [a,b]

[a] IPC – Institute for Polymers and Composites, University of Minho, Guimarães, Portugal
[b] DONE Lab – Advanced Manufacturing of Products and Tools, University of Minho, Guimarães, Portugal
[c] CMEMS-UMinho, Department of Mechanical Engineering, University of Minho, Guimarães, Portugal
[d] Department of Mechanical Engineering, University of Porto, Porto, Portugal
[e] Lab2PT, School of Architecture, University of Minho, Guimarães, Portugal

ARTICLE INFO

Keywords:
Additive manufacturing
Selective Laser Sintering
Polyamide 12
Fracture characterization
Mode I loading
Cohesive zone modelling

ABSTRACT

In recent years, parts produced by Selective Laser Sintering (SLS) technology have aroused growing interest due to their valuable potential for end-use applications. However, to ensure the applicability of SLS products for advanced structural purposes, an accurate characterization of their mechanical behaviour is essential, which includes the assessment of fracture performance. Thus, cohesive zone modelling that allows mimicking damage initiation and propagation in quasi-brittle materials is used in this work to identify the cohesive laws of Polyamide 12 parts sintered by SLS with different values of energy density. This has been accomplished with success in this work for pure mode I loading employing the Double Cantilever Beam (DCB) test. In this context, experimental data is used to evaluate the critical energy release rate under quasi-static loading, by means of the Compliance-Based Beam Method (CBBM). The identification of the cohesive laws comprises finite element analysis to achieve accurate agreement with the experimental load-displacement curves obtained under quasi-static loading. The experimental protocols are duly validated for the tested conditions, which includes a developed numerical procedure combined with experimental data.

1. Introduction

Selective Laser Sintering (SLS) is an additive manufacturing technology which produces polymeric products from powder material spread over a building platform and sintered by the thermal energy provided by a laser beam in a layer-by-layer process within a closed chamber with controlled environment (Fig. 1) [1].

As this powder bed fusion process uses a laser source to produce the parts, the degree of particle melt, the effectiveness of consolidation and the microstructural and mechanical properties of the parts are strongly influenced by the thermal energy provided during the sintering process [3-6]. A fundamental technological parameter of primary SLS process is the energy density by unit of

* Corresponding author at: IPC – Institute for Polymers and Composites, University of Minho, Guimarães, Portugal.
E-mail address: acarinalopes@dep.uminho.pt (A.C. Lopes).

https://doi.org/10.1016/j.engfracmech.2022.108555
Received 5 February 2021; Received in revised form 3 May 2022; Accepted 16 May 2022
Available online 20 May 2022
0013-7944/© 2022 Elsevier Ltd. All rights reserved.

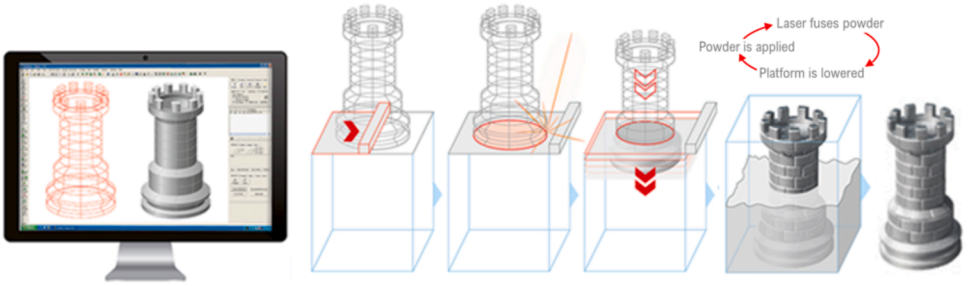

Fig. 1. Representation of SLS (Adapted from [2]).

volume, ED_V [7,8],

$$ED_V = \frac{P_{Laser}}{S_{Scan} \times D_{Hatch} \times t_{Layer}} \quad (1)$$

which depends on the laser power (P_{Laser}), scan speed (S_{Scan}), hatch distance (D_{Hatch}) and layer thickness (t_{Layer}).

In this regard, it is known that higher ED_V values ensure stronger bonds between the powder particles, resulting in SLS parts with reduced content of porosity, high density and improved mechanical performance [9–13]. However, when ED_V reaches critical values, the powder material is prone to degrade leading to yellowness parts with high content of porosity, shrinkage, low density and reduced strength [9–13].

Due to the fine compromise between mechanical properties, processability and costs under the SLS operating conditions, Polyamide 12 (PA12) thermoplastic is the most used material [14,15]. Typically, conventional PA12 exhibits high toughness with good fatigue resistance, however, due to the intrinsic content of porosity and low molecular weight of the materials in SLS, the resulting parts sometimes exhibit brittle behaviour [14,16]. Despite that, because of their great mechanical properties and considerable resistance to crack initiation and propagation, SLS parts are even more used as products of end-customer in a wide variety of applications (*e.g.,* automotive, biomedical) [14,17,18]. Thus, especially in applications where the parts are subjected to dynamic loads, the fulfilment of functional requirements become particularly relevant.

To ensure a complete and effective characterization of damage propagation in SLS parts enabling their use in advanced purposes, fracture mechanisms simulated by cohesive zone modelling should be implemented [19]. These models allow mimicking damage initiation and propagation, by following an established relationship (*i.e.,* cohesive law) between the applied stress and corresponding crack opening displacement, in homologous integration points disposed in regions of the material that are prone to undergo damage [19,20]. Therefore, several cohesive laws have been proposed to mimic damage mechanisms revealed by the materials. The most common ones exhibit the triangular shape, although the trapezoidal is also well known [21,22]. Triangular models are preferable to characterize materials that dissipate energy through a single damage mechanism, while trapezoidal models are preferable for materials with remarkable ductile behaviour and high toughness, which may be identified in tough materials that undergo plasticization behaviour [21,23]. Each of them can present alternative variants regarding the way the energy is dissipated in the post-peak regime, as two descending sections can be identified to take into account characteristic softening mechanism (*e.g.,* micro-cracking and fibre-bridging). This is accomplished by means of two branches, rather than one, turning the softening law bilinear and promoting an advantageous smoother drop [19,24].

Fracture tests can be conducted in such a way as to determine cohesive parameters. Fundamental data is required to undergo such identification, such as the load-displacement curve (P-δ curve), together with the corresponding *Resistance*-curve (R-curve). To this aim, opening mode (mode I), in-plane (mode II) and out-plane shear mode (mode III) are induced through pure loading [21,24]. To characterize materials under pure mode I, the Double Cantilever Beam (DCB) is one of the most common tests [21,25]. In the course of the loading process, two symmetric beams are progressively separated in DCB, as damage propagates from an initial crack under pure mode I loading. As the test progresses, the applied load and attained displacement are continuously recorded. Based on such results, and applying a proper data reduction scheme, R-curves representing the energy release rate (G_I) as a function of the crack length (a) can be obtained, enabling the definition of the critical energy release rate (G_{Ic}) of the material, which quantifies its resistance against a crack propagation [21].

Very few works have been published considering these fracture mechanics approaches applied in polymeric materials processed by additive manufacturing technologies. Most of the works are conducted to study the interlayers strength in extrusion-based processes, mainly with Acrylonitrile Butadiene Styrene (ABS), Polylactic Acid (PLA) and PA12 materials. A series of experiments have also been conducted in powder bed fusion processes, including SLS, although the value of G_{Ic} is not always reported. Table 1 resumes the most relevant works performed in pure mode I loading with neat and reinforced (*e.g.*, with carbon fibre (CF), glass fibre (GF), glass beads (GB), aluminium (AL)) polymeric materials processed by material extrusion, material jetting, powder bed fusion, injection moulding and hot plate press technologies.

The goal of this work is to determine the fracture toughness of PA12 processed by SLS with different ED_V values under mode I loading. Thus, several test specimens with the same dimensions were produced and properly prepared to perform DCB tests. Load-displacement curves were experimentally obtained with the same experimental protocol and the Compliance-Based Beam Method

Table 1
Mode I fracture characterization of polymeric materials.

Processing technology	Mode I test	Polymeric material	G_{Ic} (N/mm)	K_{Ic} (MPa/m$^{0.5}$)	J_c (N/mm)	Relevant conclusions	Ref.
Material extrusion	DCB	ABS	0.2–0.8	–	–	G_{Ic} increases with the temperature of extrusion.	[26]
		ABS	2.0–4.0	–	–		[27–29]
		ABS	1.4	–	–	–	[30]
		ABS	1.8	–	–	Lack of fibre-bridging in ABS-CF.	[31]
		ABS-CF	0.4	–	–		
		PLA	2.4	–	–	–	[32]
		PLA-CF	1.2	–	–		
		PLA	1.0–6.0	–	–	G_{Ic} depends on the process parameters (*e.g.*, t_{Layer}).	[33]
		PA12	0.8	–	–	A trapezoidal cohesive damage law is appropriate to	[34]
		PA12-CF	1.8	–	–	describe the non-linear behaviour of PA12.	
		PA PA-GF	1.2	–	–	Patterned surfaces promote increased G_{Ic} values comparing to flat interface profiles.	[35]
	SCB (Semi-Circular Bending)	ABS	–	–	5.9	–	[36]
		ABS	–	–	2.6–4.1	J_c tends to increase with the printing speed.	[37]
		PLA	–	–	1.8–6.8	J_c depends on the in-plane raster orientation of filaments in material extrusion. The 45/-45° orientation ensures highest fracture resistance.	[38]
Material jetting	DCB	TangoBlack Plus + VeroWhite Plus	0.2–1.0	–	–	G_{Ic} depends on the configuration of the DCB test specimen (*e.g.*, full printed or aluminium-supported).	[39,40]
Powder bed fusion	CT (Compact tension) Fatigue	PA12	N/A	–	–	The strength and heterogeneities of the internal structure of the parts influences the fracture toughness.	[17]
	DCB	PA12	N/A	–	–	The spatial configuration of the interface (*e.g.*, patterned, bulk) influences the crack propagation and the *P*-δ curves.	[41,42]
	CT	PA12	6.4	–	–	G_{Ic} depends on the testing temperature and layer *vs*	[43]
	Fracture	PA12-GB	6.7	–	–	load orientation relationship.	
		PA12	N/A	–	–	The interlayers of SLS parts are the most prone regions to undergo crack initiation and propagation.	[44]
	SENB (Single-Edge Notched Bending)	PA12	2.5–4.5	–	–	The fracture behaviour is geometry sensitive, depending on the t_{Layer}.	[45]
		PA12	–	2.7 (0°) 2.3 (90°)	–	The fracture toughness depends on the type of material and building orientation of the parts (*e.g.*,	[46]
		PA12-AL	–	1.0 (0°) 0.8 (90°)	–	0°, 90°).	
		PA12	–	2.2 (0.067 J/mm^2) 0.8 (0.034 J/mm^2)	–	The fracture toughness depends on the building orientation of the parts. It increases with the energy density provided during the sintering process.	[47,48]
	DENT (Double Edge Notched Tension)	PA12	14.1 (0°) 15.6 (90°)	–	–	G_{Ic} depends on the building orientation of the parts (*e.g.*, 0°, 90°).	[49]
Injection moulding	DCB	PA12	8.6	–	–	G_{Ic} increases with the holding time and interface temperature.	[50]
Hot plate press	DCB	PA6-CF	2.2	–	–	A trapezoidal cohesive damage law accurately determines the fracture toughness of PA6-CF.	[51]

(CBBM) was further employed to obtain the *R*-curve applied for each condition of production. The cohesive zone modelling was then accomplished, using the trapezoidal bilinear law. Good agreement was obtained with the experimental data (*i.e., P*-δ curves), which proves that damage initiation and propagation of PA12 material was well captured through this approach.

2. Materials and methods

2.1. Preparation of test specimens

The material tested in this study was an unfilled PA12 powder, the PA2200 from EOS Electro Optical Systems GmbH, in a mixture ratio of 50% of previously processed material with 50% of new pristine material. Test specimens with nominal dimensions $L = 150$ mm, $B = 5$ mm and $2h = 20$ mm (Fig. 2) were horizontally produced with holes (diameter: 3 mm) in the centre of the building platform of the EOS P 396 equipment.

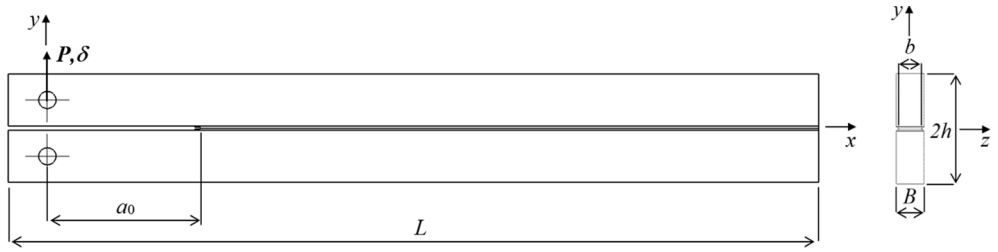

Fig. 2. Geometric configuration of the DCB test specimen using loading holes.

Table 2
SLS process parameters considered for the sintering.

POSITION AND ORIENTATION OF SLS TEST SPECIMENS ON THE EOS P 396 BUILDING PLATFORM		
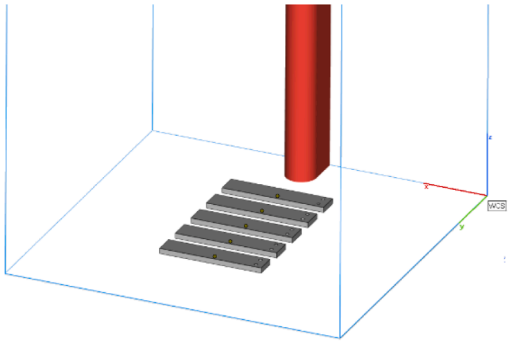		
Process temperature (°C)		173
Warm up temperature (°C)		160
Removal chamber temperature (°C)		130
Layer thickness (mm)		0.12
Beam offset (mm)		0.32
Hatch distance (mm)		0.30
Contour and post-contour	Laser power (W)	34
	Scan speed (mm/s)	3000
	Laser power (W)	20
Edges and post-edges	Scan speed (mm/s)	1500

In order to evaluate the influence of the most relevant SLS operating parameters on G_{Ic}, the test specimens were produced with ED_V values ranging from 0.158 J/mm^3 to 0.358 J/mm^3 at constant intervals of 0.04 J/mm^3, depending on different P_{Laser} and S_{Scan} combinations. Parameters from the initial preheating phase, contour and post-contour, edges and post-edges were fixed in the standard mode (Table 2).

According to the material datasheet, for standard conditions of production, the PA12 parts present an elastic modulus of 1650 MPa,

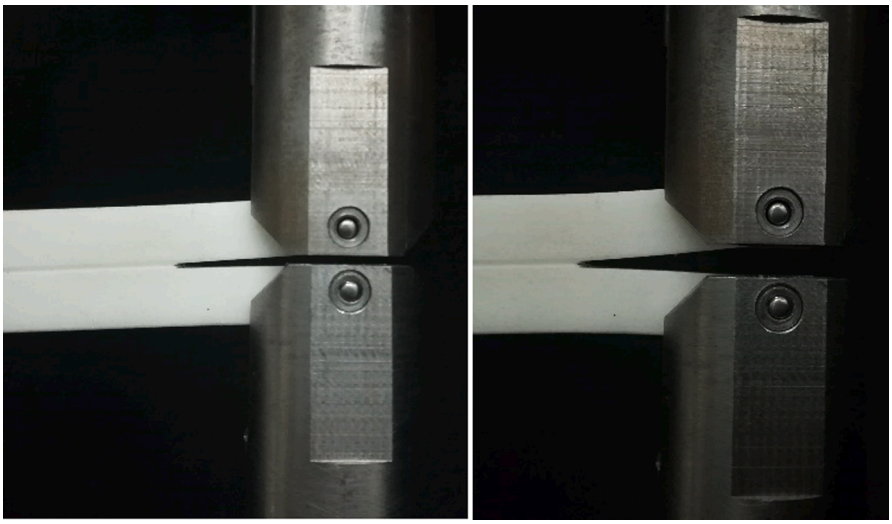

Fig. 3. Experimental setup of DCB evidencing crack propagation.

Fig. 4. Representative surface of crack propagation at the end of the DCB test.

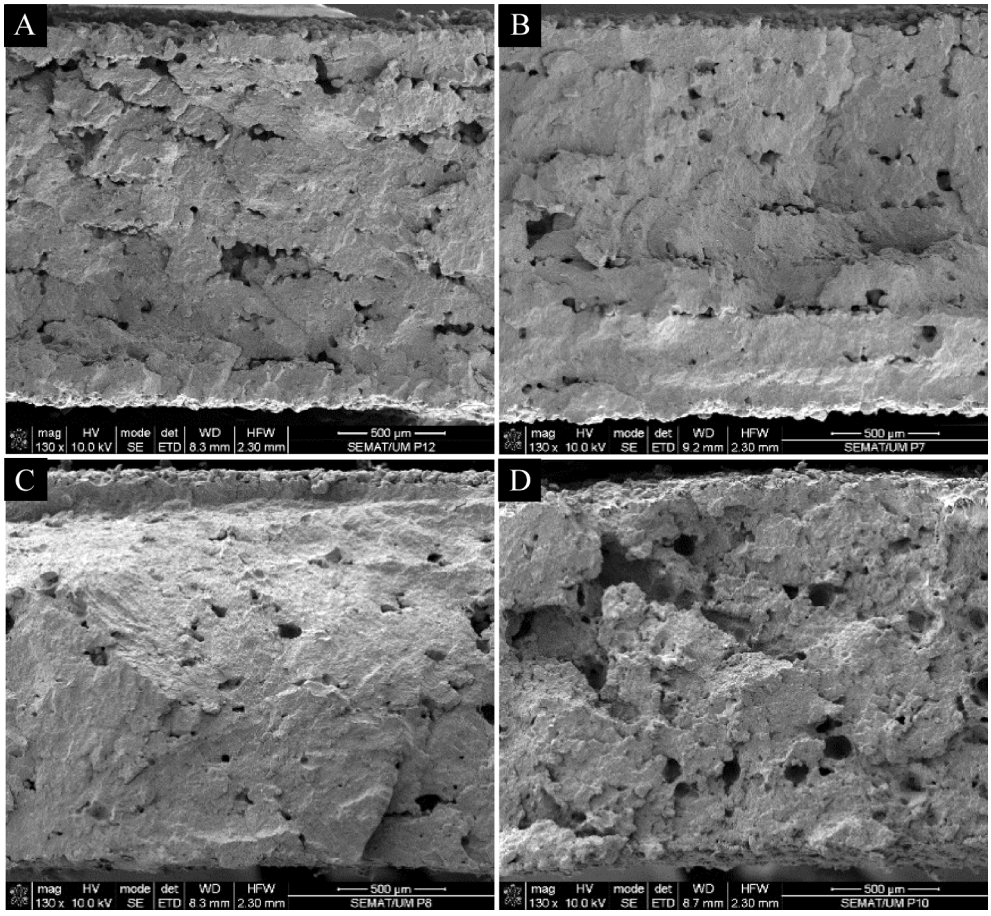

Fig. 5. SEM images showing the cross-section of SLS test specimens produced with ED_V of (A) 0.158 (B) 0.198 (C) 0.278 (D) 0.358 J/mm^3.

a tensile strength of 48 MPa, a tensile strain at break of 18% and a flexural modulus of 1500 MPa [52].

After the sintering process, three test specimens per condition were prepared for DCB in a Bridgeport® milling machine with a fine cut to present the same initial crack length (a_0). Hence, a ceramic cutting blade (thickness: 0.8 mm) was first used to prepare an initial length of 27.3 mm. The crack length was further extended by means of a thin sharp cutter (thickness: 0.4 mm) rigidly set to the machine crosshead, with a displacement rate equal to 50 mm/min. This procedure was executed with a pristine cutter blade, to prevent damage onset ahead of the crack tip prior to fracture test. A lateral notch was additionally made in both sides of the specimen at half-height (depth: 0.5 mm) using a metal cutting blade (thickness: 1.2 mm; cut angle: 70°). This singularity prevents crack deflection in the course of the loading process, thus assuring mode I loading during propagation. This protocol allowed to produce an initial crack length (a_0) of 28.3 mm.

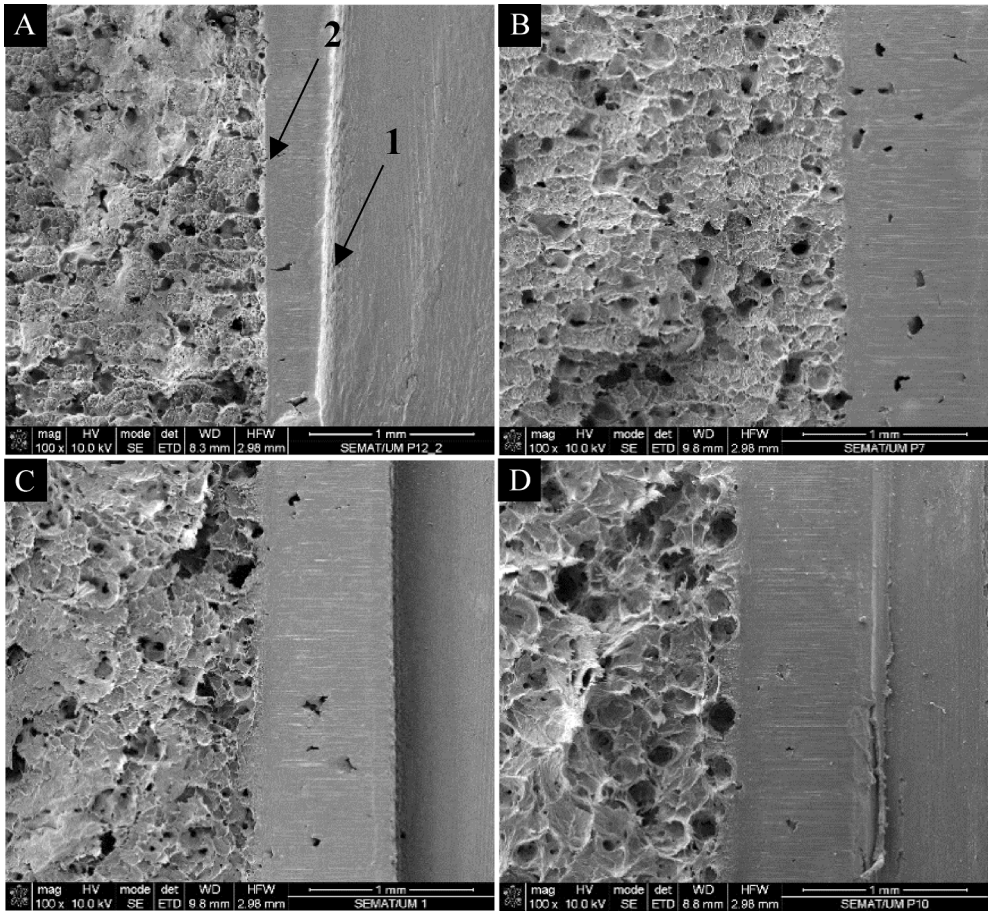

Fig. 6. SEM images showing the morphology of the cracked region of SLS test specimens produced with ED_V of (A) 0.158 (B) 0.198 (C) 0.278 (D) 0.358 J/mm^3.

2.2. Mechanical tests

The DCB tests were performed in an INSTRON® 5969 Universal Testing System with a load-cell of 5 kN at room temperature. The tests were conducted at 3.6 mm/min to ensure a consistent and stable crack propagation with reduced mechanisms of viscoelasticity (less than 3 min to attain the peak load on average). In all experiments, the applied load and displacement were continuously recorded with an acquisition rate of 10 Hz to obtain the *P-δ* curves. The evolution of the crack length was not directly monitored during the test, due to difficulties in the definition of the crack tip in this material, which is owed to the development of a non-negligible fracture process zone at the crack tip. To guarantee that crack propagates under pure mode I loading, all test specimens were carefully positioned and aligned according to the experimental setup shown in Fig. 3.

Fig. 4 shows the fractured region obtained in the experiments.

Fig. 5 presents Scanning Electron Microscopy (SEM) micrographs of the cross-section (*i.e.*, normal to *x*-axis, according to Fig. 2) obtained from a liquid nitrogen cut of SLS test specimens produced with different ED_V values. In accordance with the literature, when the energy supplied by the laser beam to the powder particles is low, namely between 0.158 J/mm^3 and 0.198 J/mm^3, the consolidation and compaction of the powder particles across the building layers are not completely achieved (Fig. 5 A and B). Those discontinuities combined with the intrinsic content of porosity at lower ED_V values allow easier crack initiation and propagation, as proved before by Brugo T. *et al.* [44]. The cross-section of the specimens becomes homogenous when ED_V increases until 0.318 J/mm^3 (Fig. 5 C). On the other hand, when ED_V reaches the high critical value of 0.358 J/mm^3, the powder particles are prone to degrade and compromise the quality of the corresponding cross-section (Fig. 5 D) [9].

Fig. 6 shows a set of SEM micrographs of cracked surfaces of the corresponding test specimens produced with ED_V values of 0.158 J/mm^3, 0.198 J/mm^3, 0.278 J/mm^3 and 0.358 J/mm^3. It clearly allows to distinguish three different sections delimited by the initial notch (line 1 in Fig. 6), the pre-crack prepared with the thin sharp cutter (line 2 in Fig. 6), and the surface of crack propagation under pure mode I loading. The results suggest that the content of porosity evidenced on the surface of propagation may be a vital factor influencing the critical energy release rate, G_{Ic}, of the specimen depending on the ED_V value used in its production.

Regardless of the operating parameters considered for the sintering process, the test specimens exhibited *P-δ* curves (Fig. 7) with

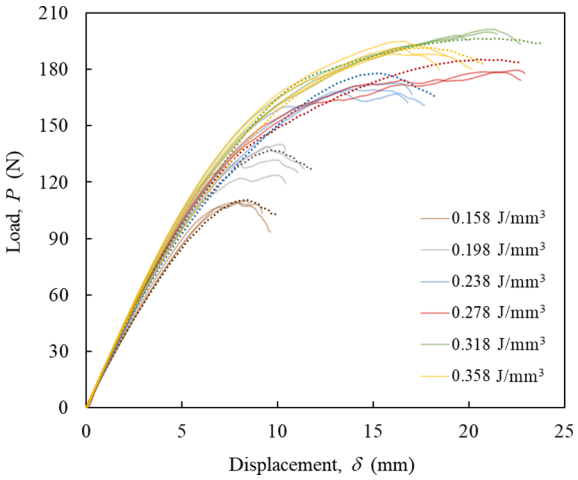

Fig. 7. Experimental and numerical P-δ curves of SLS test specimens depending on ED_V. Dotted-line refers to numerical data.

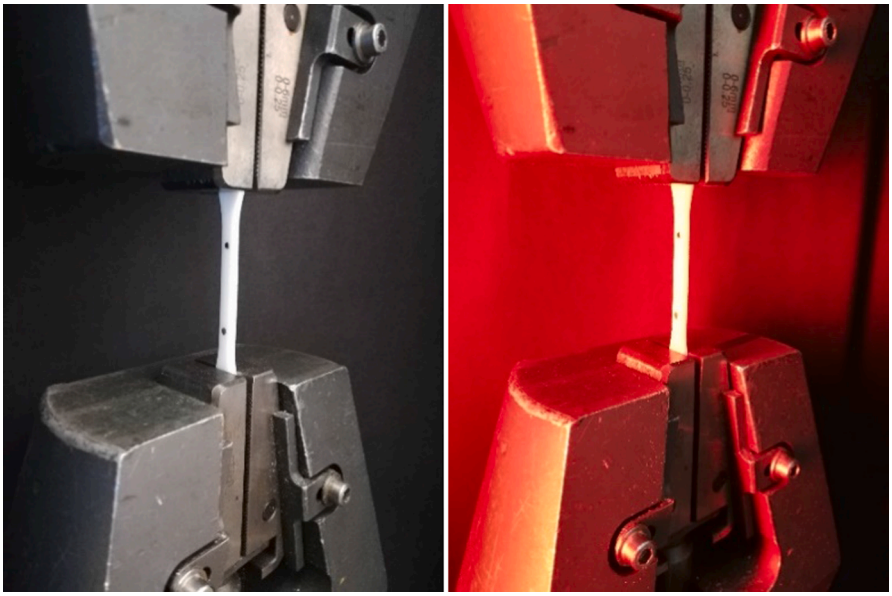

Fig. 8. Tensile tests of SLS test specimens (type 1BA, ISO 527-2).

some non-linearity after the peak-load, putting into evidence the existence of pores in the microstructure. It is also visible that ED_V influences the material resistance, although the initial compliance is not affected.

Another study was conducted to evaluate the material strength under tensile loading, using test specimens (type 1BA, ISO 527-2) produced with the SLS process parameters presented in Table 2 and the corresponding values of ED_V (*i.e.*, within the interval 0.158 J/mm^3 to 0.358 J/mm^3). The specimens were tested in an INSTRON® 5969 Universal Testing System with video extensometer using a load-cell of 5 kN at a rate of 10 mm/min at room temperature (Fig. 8).

2.3. Compliance-Based Beam method (CBBM)

Considering that in this work the evolution of crack propagation was not directly and quantitatively recorded during the DCB tests, the Compliance-Based Beam Method (CBBM) proposed by Moura *et al.* [24] was used as a data reduction scheme to evaluate the fracture toughness under mode I loading. This method allows the determination of the R-curve, *i.e.,* the energy release rate, G_I, as a function of an equivalent crack length, a_e, considering the current compliance of the specimen, C [19,24].

Thus, based on this method and considering the Timoshenko beam theory, the elastic strain energy of a specimen, U, including the flexural and shear components (see Fig. 2), is given by [24]:

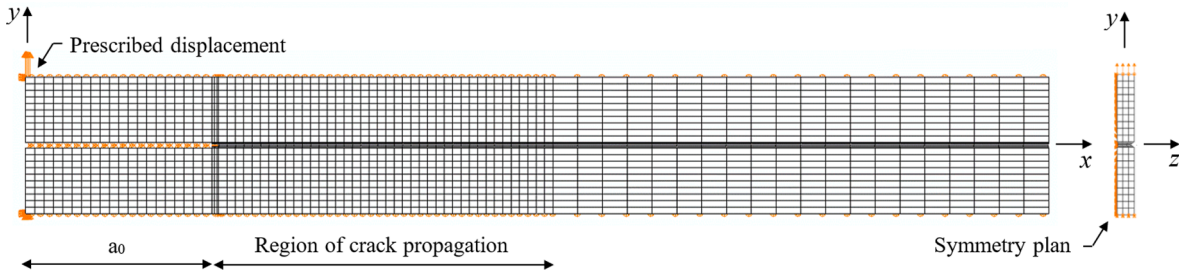

Fig. 9. Mesh and boundary conditions used in the numerical analysis.

$$U = 2\left[\int_0^a \frac{M_f^2}{2EI}dx + \int_0^a \int_{-h/2}^{h/2} \frac{\tau^2}{2G}Bdydx\right] \tag{2}$$

where M_f is the bending moment, I the second moment of area, τ the shear stress, B the specimen width in the cracked region, a the current crack length, h the specimen half-height, E the elastic modulus and G the shear modulus of the material [24]. Then, considering the Castigliano theorem and Eq. (2), the resulting displacement is obtained from Eq. (3) as follows [24]:

$$\delta = \frac{dU}{dP} = \frac{8Pa^3}{EBh^3} + \frac{12Pa}{5BhG} \tag{3}$$

with P standing for the load applied on the specimen. Taking into account Eq. (3), the specimen compliance $C = \delta/P$ can be obtained [19]:

$$C = \frac{8a^3}{EBh^3} + \frac{12a}{5BhG} \tag{4}$$

This method supposes the determination of a_e, which considers the effect of the fracture process zone at the crack tip, influencing the P-δ curve profile. The analytical solution of Eq. (4) for the equivalent crack length, a_e, is obtained by [24]:

$$a_e = \frac{1}{6\alpha}A - \frac{2\beta}{A} \tag{5}$$

with α, β and A defined according to [24]:

$$\alpha = \frac{8}{Bh^3E}; \beta = \frac{12}{5BhG}; A = \left(\left(108C + 12\sqrt{3\left(\frac{4\beta^3 + 27C^2\alpha}{\alpha}\right)}\right)\alpha^2\right)^{\frac{1}{3}} \tag{6}$$

The energy release rate, G_I, is computed using the Irwin-Kies equation [24]:

$$G_I = \frac{P^2}{2b}\frac{dC}{da} \tag{7}$$

Finally, the combination of Eqs. (4) and (7) yields [24]:

$$G_I = \frac{6P^2}{Bbh}\left(\frac{2a_e^2}{Eh^2} + \frac{1}{5G}\right) \tag{8}$$

which was adapted to account for the reduction of width (*i.e.*, parameter b) following the production of the lateral notches [19,24].

In this work, E was numerically determined based on the initial compliance, by fitting the elastic region of the numerical P-δ curve to the experimental one. Regarding G, although it is reported in the literature that a typical value can be used, it was determined according to E and Poisson's ratio (ν) of each test specimen [24], due to the isotropic nature of this material.

In fact, the CBBM is a suitable method which includes effects of the energy dissipated in the fracture process zone and does not require the direct monitoring of the crack length during the test [21,53]. In this work its use had two main purposes. The first one was to reproduce the R-curve from the experimental results in order to estimate the critical strain energy release rate, G_{Ic} value (*i.e.,* the plateau of the R-curve), to introduce in the numerical simulations. The second one was to validate the experimental protocol, *i.e.,* the geometric parameters selected for the study.

2.4. Numerical analysis

The numerical analysis was conducted considering the real dimensions of the specimen with the geometrical configuration presented in Fig. 2. Due to the attainment of a non-negligible plateau in the experimental P-δ curves (Fig. 7), the numerical analysis was performed using a bilinear trapezoidal cohesive damage law with the purpose to simulate the crack initiation and propagation of the

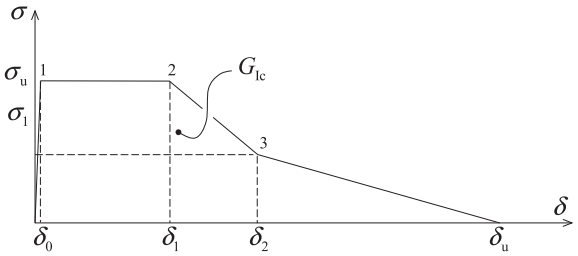

Fig. 10. Trapezoidal bilinear softening CL.

SLS test specimens. The numerical model considered in the finite element analysis used linear 8-nodes hexahedral elements. To simplify the analysis and to reduce the computational effort, only a half-width of the specimen was considered with a mesh particularly refined in the region of crack propagation, thus allowing to improve the accuracy of the analysis in that region. Therefore, the total mesh comprised 83 elements along the *x*-axis, 28 elements along the *y*-axis and 6 elements along the *z*-axis (Fig. 9). The boundary conditions were properly imposed according to the experimental tests. A small load displacement was considered to allow smooth and stable crack initiation and propagation in the course of the loading process.

Based on a suitable range of elastic modulus capable to accurately reproduce the experimental elastic compliance of the data, the PA12 test specimens produced by SLS were simulated considering an isotropic material with $\nu = 0.3$ and E ranging from 1516.7 MPa to 1716.7 MPa depending on the ED_V value.

2.5. Cohesive modelling

Based on the profile of the experimental *P*-δ curves, a searching procedure based on finite element modelling was employed using a trapezoidal bilinear softening cohesive law (CL) (Fig. 10). It should be noted that this law can replicate both the linear and bilinear CL, by proper definition of the defining parameters (*i.e.*, position of points 2 and 3 aligned with corresponding positions of point 1 and δ_u).

The most relevant equations of this CL were previously developed and presented in [54] by Silva et al. Thus, considering k as the stiffness of the interface assumed equal to 10^6 N/mm^3, the first ascending region of the curve, *i.e.,* for $\delta < \delta_0$, is described by [54]:

$$\sigma(\delta) = k\delta \tag{9}$$

Then, when the local strength, σ_u, is achieved, damage mechanisms occur, and the reduction of stiffness is given by [54]:

$$\sigma(\delta) = (1-d)k\delta \tag{10}$$

where d is a parameter that quantifies the damage developed ahead of the crack tip, which ranges from 0 at δ_0 to 1 at δ_u. In the plateau of the cohesive model, the stiffness slightly decreases according to [54]:

$$d = 1 - \frac{\delta_0}{\delta} \tag{11}$$

Finally, considering the bilinearity of the CL defined by two branches after the post-peak region, Eqs. (12) and (13) are respectively applied to the first (*i.e.,* $\delta_1 < \delta < \delta_2$) and second (*i.e.,* $\delta_2 < \delta < \delta_u$) descending sections [54]:

$$d = 1 - \frac{\frac{\sigma_2}{k}(\delta - \delta_1) + \delta_0(\delta_2 - \delta)}{\delta(\delta_2 - \delta_1)} \tag{12}$$

$$d = 1 - \frac{\sigma_2(\delta_u - \delta)}{k\delta(\delta_u - \delta_2)} \tag{13}$$

The parameters which define the shape of this CL were obtained in this research through a searching method based on the agreement of the experimental and numerical *P*-δ curves.

3. Results and discussion

Following the experimental tests, the first step of the study was to numerically determine the elastic modulus of each DCB test specimen. Then, considering the attained values, the CBBM (Section 2.3) was used to determine the corresponding value of G_{Ic}. The remaining parameters to obtain the bilinear trapezoidal CL were determined through the numerical-experimental agreement of the *P*-δ curves, combining finite element analysis and experimental data. The obtained *P*-δ curves were then used to plot the corresponding *R*-curves using the CBBM, as a way to prove that the method is accurate and robust.

Fig. 11 presents the plots of average true stress-strain curves obtained from tensile tests (cf. Fig. 8). The data allow to evaluate the tensile global strength of PA12 parts produced by SLS with ED_V values ranging from 0.158 J/mm^3 to 0.358 J/mm^3.

The results demonstrated that the mechanical properties obtained under uniaxial tensile loading increase with ED_V until 0.318 J/

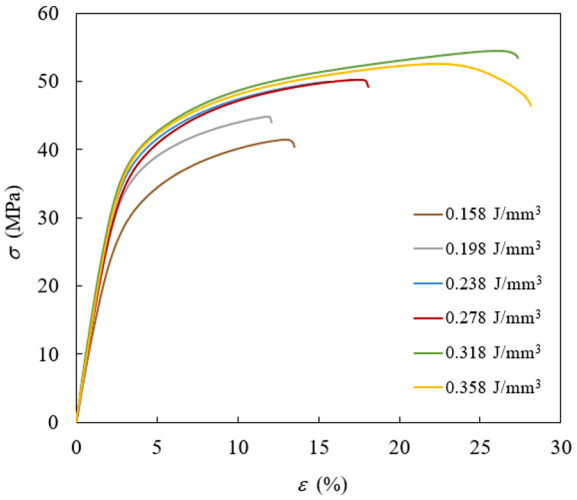

Fig. 11. True stress-strain curves of SLS test specimens depending on ED_V.

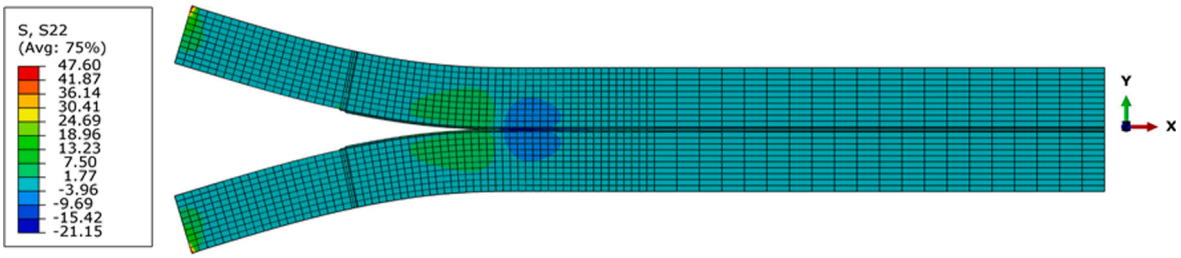

Fig. 12. Normal stress (σ_y) field along *x*-direction (in MPa) of the DCB test specimen produced with 0.238 J/mm^3 evidencing the crack propagation.

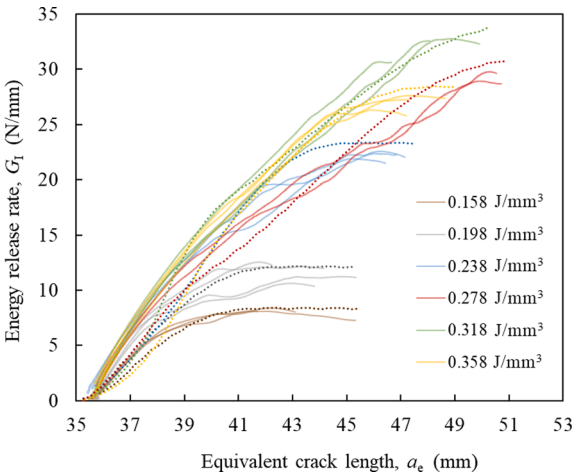

Fig. 13. Experimental and numerical *R*-curves of SLS test specimens depending on ED_V. Dotted-line refers to numerical data.

mm^3 recording 11% higher tensile strength in relation to the lowest energy level (*i.e.,* 0.158 J/mm^3). In turn, the test specimens produced with 0.358 J/mm^3 exhibited reduced mechanical performance. This agrees with results of previous works that showed that the tensile properties increase until a machine-specific critical value from which overheating begins [55,56].

Fig. 12 shows the profile of the normal stress field (σ_y) along *x*-direction (in MPa) obtained in the numerical analysis with the set of cohesive parameters defined for a medium level of energy, *i.e.*, 0.238 J/mm^3, that allowed mimicking the corresponding *P*-δ curves shown in Fig. 7.

The results prove that the areas of the test specimen away from the region of crack propagation are not directly affected by the

Table 3
Elastic modulus and parameters of the trapezoidal bilinear softening CL.

ED_V (J/mm^3)	E (MPa)	G_{Ic} (N/mm)	σ_u (MPa)	δ_1 (mm)	σ_1 (MPa)	δ_2 (mm)
0.158	1516.70	8.10	12.00	0.25	9.00	0.35
0.198	1650.00	11.70	16.00	0.10	10.00	0.40
0.238	1616.70	22.20	15.00	0.05	11.00	0.40
0.278	1687.50	29.10	16.00	0.05	5.50	1.00
0.318	1700.00	32.00	14.00	0.60	4.50	1.60
0.358	1716.70	26.90	12.00	0.60	6.00	1.60

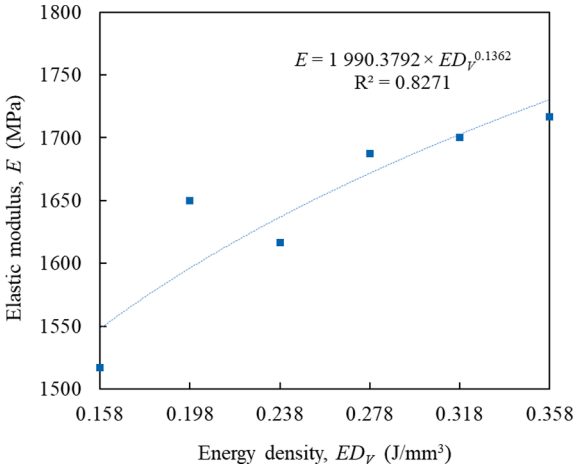

Fig. 14. Elastic modulus of SLS test specimens as a function of ED_V.

unidirectional *y*-loading and, therefore, exhibit a practically null stress field. In contrast, a compressive and tensile stress field is developed in the region of crack propagation. In this regard, the data reveal a tensile stress in the range of 7.5–18.96 MPa in the vicinity of the crack tip dictating the size of the cohesive zone length, l_{CZ}, followed by a region of compressive normal stresses resulting from the specimen arms curvature.

Fig. 13 shows the numerical-experimental agreement of the *R*-curves, based on the corresponding numerical-experimental *P*-δ curves shown in Fig. 7.

The results demonstrate the suitability of the applied searching method of the numerical simulations to evaluate the proposed procedure under pure mode I loading, since a good numerical-experimental agreement was established for all conditions. In the *P*-δ curves (Fig. 7) it is possible to verify that although the initial elastic compliance of all test specimens is similar, the region corresponding to the peak-load puts into evidence that when ED_V increases, the load for same values of displacement tends to increase, which has a direct effect on the local cohesive strength under mode I loading, $\sigma_{u,I}$ and on the fracture energy, G_{Ic}. In the corresponding *R*-curves (Fig. 13), it is possible to detect an initial growing trend of the energy release rate, G_I, which is due to the development of the fracture process zone that occurs before crack initiation. That growing trend typically occurs at higher rates when ED_V increases. After that, a pronounced plateau is presented, which is intrinsically related with the post-peak region of the *P*-δ curves, corresponding to crack propagation. Table 3 reports the parameters of the trapezoidal bilinear softening CL that allowed to obtain the numerical-experimental agreement of each condition. According to Table 3, E gradually increases with ED_V from 1516.7 MPa in the condition of lowest energy to 1716.7 MPa in the condition of highest energy, according to the power law shown in Fig. 14. This denotes an increase of 13% in the elastic modulus of the system at a variation of 0.20 J/mm^3 in the energy supplied during the sintering.

Moreover, Table 3 reveals that G_{Ic} increases from 8.1 N/mm in test specimens produced with 0.158 J/mm^3 to 32 N/mm in test specimens produced with 0.318 J/mm^3. It represents a difference of 395% in the mode I fracture toughness of SLS parts when the energy supplied during the sintering process increases 0.16 J/mm^3. After 0.318 J/mm^3, a downward trend until 26.9 N/mm is verified in test specimens produced with 0.358 J/mm^3. These results are in accordance with the global tensile strength plotted in Fig. 11 and the morphological characteristics shown in Figs. 5 and 6. In this regard, previous studies have shown that the presence of defects in the midplane section of the test specimens can decrease G_{Ic} by more than 23% in relation to a defect-free solution due to the different capacity for energy absorption [57]. In summary, it was proved that the cohesive parameters defining the trapezoidal bilinear law for pure mode I loading of PA12 parts produced by SLS are dependent on the ED_V value. In this regard, the analysis shows that medium-high ED_V values are desired to achieve great fracture toughness until a high critical value of 0.318 J/mm^3. Above this value, the fracture toughness is negatively affected.

Fig. 15 shows the evolution of the cohesive zone length, l_{CZ}, as a function of the equivalent crack length, a_e, for each condition of

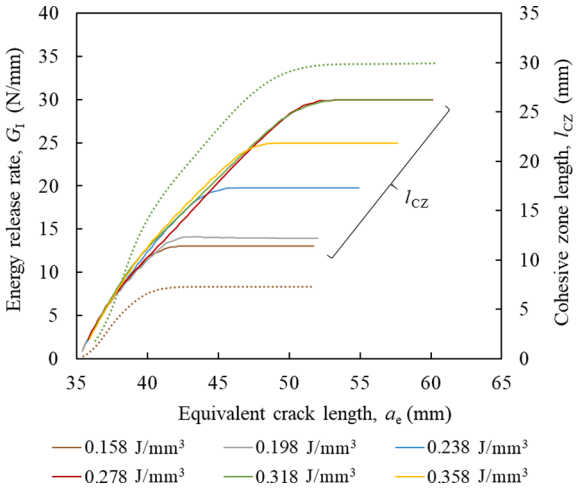

Fig. 15. Evolution of l_{CZ} as a function of a_e of SLS test specimens depending on ED_V. Dotted-line refers to *R*-curves.

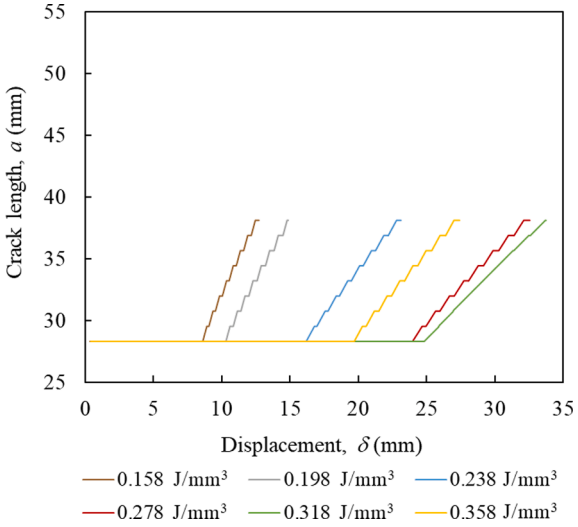

Fig. 16. Evolution of a as a function of δ of SLS test specimens depending on ED_V.

production in terms of ED_V, together with two numerical *R*-curves for extreme values of G_{Ic}. It is visible that l_{CZ} increases in the initial stage of the loading process, revealing a critical size l_{CZc} in the final phase before total rupture. This behaviour is characteristic of the DCB test, and it is an essential condition to obtain accurate values of the critical strain energy release rate under mode I loading, G_{Ic} (*i.e.*, self-similar crack propagation). Fig. 15 also reveals that the variation of l_{CZc} with ED_V is consistent with the trend obtained for G_{Ic} (Fig. 13).

In turn, Fig. 16 shows the evolution of the numerical crack length, a, as a function of the applied displacement, δ, for each value of ED_V. The results prove that when G_{Ic} increases, the crack propagation occurs at high displacement loading values and the corresponding cohesive zone length l_{CZ} is extended (Fig. 15).

The variation of l_{CZ} along the reduced specimen width (*i.e.,* dimension b in Fig. 2), l_{CZz}, proves that the studied system is almost insensitive to the edge effect, excepting the highest ED_V of 0.358 J/mm^3 that exhibits a slight l_{CZz} variation of 1.23 mm between the middle and the outer edges of the test specimen (Fig. 17).

Considering a medium level of energy (*i.e.*, 0.238 J/mm^3), numerical studies were further conducted in order to evaluate the influence of the initial crack length (a_0) on the fracture toughness of the system. To this aim, the cohesive parameters and the elastic properties of the elected SLS test specimen were combined with different a_0 values, including 27.3 mm, 27.8 mm, 28.3 mm (used in this work), 28.8 mm and 29.3 mm, using the same increment of displacement. The numerical *P*-δ curves and the corresponding *R*-curves are presented in Fig. 18.

The *P*-δ curves allow to verify that the initial compliance of the test specimens increases with a_0. It has a direct effect on the initial growing trend of the energy release rate of the corresponding *R*-curves. However, as can be seen by the horizontal asymptote, G_{Ic} is

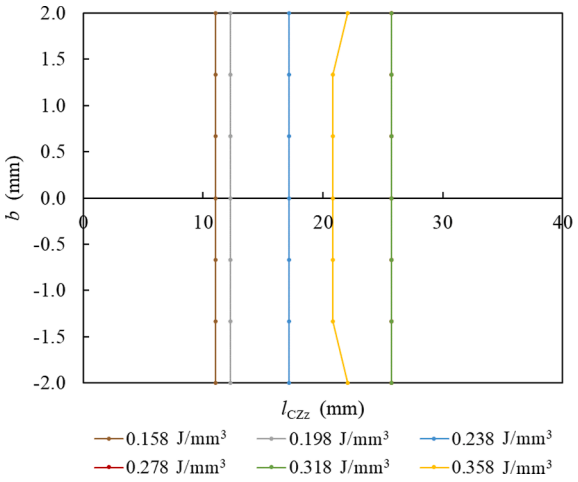

Fig. 17. Evolution of l_{CZz} along b of SLS test specimens depending on ED_V.

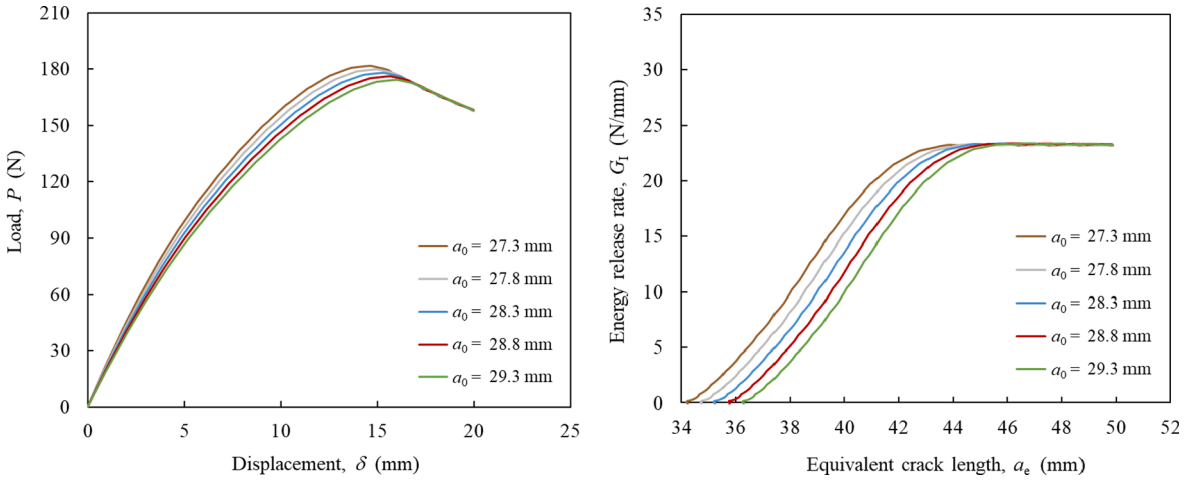

Fig. 18. Numerical P-δ curves and R-curves of SLS test specimens considering different a_0 values.

insensitive to a_0, within the tested range of values. It proves that G_{Ic} is characteristic and dependent on the material and, therefore, independent of the geometric configuration of the test specimen.

4. Conclusions

Selective Laser Sintering (SLS) is a powder bed fusion process with high potential to produce polymeric parts for structural applications. However, the complete applicability of SLS is limited due to the unfused powder particles, porosity and other morphological defects developed in the parts during the sintering process. These critical factors influence the resulting mechanical performance and make difficult to ensure the operational requirements of end-use products submitted to dynamic loads.

In this work, PA12 material processed by SLS with different ED_V values was experimentally and numerically characterized under pure mode I loading through DCB tests. The good numerical-experimental agreement obtained proved the suitability of the applied methodology to identify the cohesive parameters of the trapezoidal bilinear softening CL, allowing to successfully reproduce the fracture toughness of the studied system under pure mode I loading. The results showed that the fracture toughness tends to increase with ED_V, from low to medium-high values of energy. However, when ED_V is critical high, the morphological structure of the parts is compromised, and the tensile global strength and critical energy release rate (G_{Ic}) are reduced. Despite that, the high G_{Ic} values identified in this work prove the reliability of this material and technology in applications where high mechanical performance is required, considering G_{Ic} as a design criterion.

In future work, PA12 parts produced by SLS will be tested with other loading modes, including in-plane and out-plane shear. Atmospheric conditioning procedures before testing will also be implemented in order to prevent the influence of the PA12 thermo-hygroscope behaviour on the rigorous determination of its fracture toughness.

CRediT authorship contribution statement

A.C. Lopes: Investigation, Methodology, Visualization, Writing – original draft, Writing – review & editing, Data curation. **E.C. Silva:** Investigation, Methodology, Visualization, Writing – original draft, Writing – review & editing, Data curation. **N. Dourado:** Conceptualization, Investigation, Methodology, Software, Supervision, Validation, Writing – original draft. **M.F.S.F. de Moura:** Conceptualization, Investigation, Methodology, Software, Supervision, Validation, Writing – original draft. **A.M. Sampaio:** Formal analysis, Funding acquisition, Project administration, Supervision, Validation, Writing – original draft. **A.J. Pontes:** Formal analysis, Funding acquisition, Project administration, Supervision, Validation, Writing – original draft.

Declaration of Competing Interest

The authors declare that they have no known competing financial interests or personal relationships that could have appeared to influence the work reported in this paper.

Acknowledgments

The authors acknowledge the financial support given by FCT through the reference PhD research scholarship 2020.04520.BD, the reference projects UID/CTM/50025/2019 and UID/EEA/04436/2019, the European Structural and Investment Funds in the FEDER component, through the Operational Competitiveness and Internationalization Programme (COMPETE 2020) [Project n° 037902; Funding Reference: POCI-01-0247-FEDER-037902], the 'Laboratório Associado de Energia, Transportes e Aeronáutica' (LAETA) through the project UID/EMS/50022/2019 and the FCT/MCTES through national funds (PIDDAC).

References

[1] ASTM. ASTM F2792 12a - Standard Terminology for Additive Manufacturing Technologies; 2012.
[2] EOS GmbH. Additive Manufacturing, Laser-Sintering and Industrial 3D Printing - Benefits and Functional Principle; 2019. https://www.eos.info/additive_manufacturing/for_technology_interested [accessed July 18, 2019].
[3] Kiani A, Khazaee S, Badrossamay M, Foroozmehr E, Karevan M. An Investigation into Thermal History and Its Correlation with Mechanical Properties of PA12 Parts Produced by Selective Laser Sintering Process. J Mater Eng Perform 2020;29(2):832–40. https://doi.org/10.1007/s11665-020-04640-0.
[4] Wörz A, Wudy K, Drummer D, Wegner A, Witt G. Comparison of long-term properties of laser sintered and injection molded polyamide 12 parts. J Polym Eng 2018;38:573–82. https://doi.org/10.1515/polyeng-2017-0227.
[5] Majewski C, Zarringhalam H, Hopkinson N. Effect of the degree of particle melt on mechanical properties in selective laser-sintered Nylon-12 parts. Proc Inst Mech Eng Part B J Eng Manuf 2008;222(9):1055–64. https://doi.org/10.1243/09544054JEM1122.
[6] Pavan M, Faes M, Strobbe D, Van Hooreweder B, Craeghs T, Moens D, et al. On the influence of inter-layer time and energy density on selected critical-to-quality properties of PA12 parts produced via laser sintering. Polym Test 2017;61:386–95. https://doi.org/10.1016/j.polymertesting.2017.05.027.
[7] Beitz S, Uerlich R, Bokelmann T, Diener A, Vietor T, Kwade A. Influence of Powder Deposition on Powder Bed and Specimen Properties. Materials 2019;12(2):297. https://doi.org/10.3390/ma12020297.
[8] Hofland EC, Baran I, Wismeijer DA. Correlation of Process Parameters with Mechanical Properties of Laser Sintered PA12 Parts. Adv Mater Sci Eng 2017;2017:1–11. https://doi.org/10.1155/2017/4953173.
[9] Ho HCH, Gibson I, Cheung WL. Effects of energy density on morphology and properties of selective laser sintered polycarbonate. J Mater Process Technol 1999;89–90:204–10. https://doi.org/10.1016/S0924-0136(99)00007-2.
[10] Dewulf W, Pavan M, Craeghs T, Kruth J-P. Using X-ray computed tomography to improve the porosity level of polyamide-12 laser sintered parts. CIRP Ann - Manuf Technol 2016;65(1):205–8. https://doi.org/10.1016/j.cirp.2016.04.056.
[11] Wu J, Xu X, Zhao Z, Wang M, Zhang J. Study in performance and morphology of polyamide 12 produced by selective laser sintering technology. Rapid Prototyp J 2018;24(5):813–20. https://doi.org/10.1108/RPJ-01-2017-0010.
[12] Beard MA, Ghita OR, Evans KE. Monitoring the Effects of Selective Laser Sintering (SLS) Build Parameters on Polyamide Using Near Infrared Spectroscopy. J Appl Polym Sci 2011;121(6):3153–8.
[13] Ling Z, Wu J, Wang X, Li X, Zheng J. Experimental study on the variance of mechanical properties of polyamide 6 during multi-layer sintering process in selective laser sintering. Int J Adv Manuf Technol 2019;101(5-8):1227–34. https://doi.org/10.1007/s00170-018-3004-8.
[14] Salazar A, Rico A, Rodríguez J, Segurado Escudero J, Seltzer R, Martin de la Escalera Cutillas F. Martin De La Escalera Cutillas F. Fatigue crack growth of SLS polyamide 12: Effect of reinforcement and temperature. Compos Part B Eng 2014;59:285–92.
[15] Crespo M, Gómez-del Río MT, Rodríguez J. Failure of SLS polyamide 12 notched samples at high loading rates. Theor Appl Fract Mech 2017;92:233–9. https://doi.org/10.1016/j.tafmec.2017.08.008.
[16] Seltzer R, de la Escalera FM, Segurado J. Effect of water conditioning on the fracture behavior of PA12 composites processed by selective laser sintering. Mater Sci Eng, A 2011;528(22-23):6927–33. https://doi.org/10.1016/j.msea.2011.05.045.
[17] Blattmeier M, Witt G, Wortberg J, Eggert J, Toepker J. Influence of surface characteristics on fatigue behaviour of laser sintered plastics. Rapid Prototyp J 2012;18:161–71. https://doi.org/10.1108/13552541211212140.
[18] Van Hooreweder B, De Coninck F, Moens D, Boonen R, Sas P. Microstructural characterization of SLS-PA12 specimens under dynamic tension/compression excitation. Polym Test 2010;29(3):319–26. https://doi.org/10.1016/j.polymertesting.2009.12.006.
[19] Pereira FAM, de Moura MFSF, Dourado N, Morais JJL, Xavier J, Dias MIR. Direct and inverse methods applied to the determination of mode I cohesive law of bovine cortical bone using the DCB test. Int J Solids Struct 2017;128:210–20. https://doi.org/10.1016/j.ijsolstr.2017.08.028.
[20] Dourado N. R-Curve behaviour and size effect of a quasibrittle material: Wood. Universidade de Trás-os Montes e Alto Douro and Université Bordeaux I; 2008.
[21] Chaves FJP, da Silva LFM, de Moura MFSF, Dillard DA, Esteves VHC. Fracture mechanics tests in adhesively bonded joints: A literature review. J Adhes 2014;90(12):955–92. https://doi.org/10.1080/00218464.2013.859075.
[22] Huang D, Sheng B, Shen Y, Chui YH. An analytical solution for double cantilever beam based on elastic–plastic bilinear cohesive law: Analysis for mode I fracture of fibrous composites. Eng Fract Mech 2018;193:66–76. https://doi.org/10.1016/j.engfracmech.2018.02.019.
[23] da Silva LFM, Campilho RDSG. Advances in numerical modelling of adhesive joints. Springer; 2012.
[24] de Moura MFSF, Morais JJL, Dourado N. A new data reduction scheme for mode I wood fracture characterization using the double cantilever beam test. Eng Fract Mech 2008;75(13):3852–65. https://doi.org/10.1016/j.engfracmech.2008.02.006.
[25] Dourado NMM, de Moura MFS f., Morais JJL, Silva MAL. Estimate of resistance-curve in wood through the double cantilever beam test. Holzforschung 2010;64:119–26. https://doi.org/10.1515/HF.2010.010.

[26] Barile C, Casavola C, Cazzato A. Acoustic Emissions in 3D Printed Parts under Mode I Delamination Test. Materials 2018;11:1760. https://doi.org/10.3390/ma11091760.
[27] Aliheidari N, Tripuraneni R, Ameli A, Nadimpalli S. Fracture resistance measurement of fused deposition modeling 3D printed polymers. Polym Test 2017;60:94–101. https://doi.org/10.1016/j.polymertesting.2017.03.016.
[28] Aliheidari N, Tripuraneni R, Hohimer C, Christ J, Ameli A. The impact of nozzle and bed temperatures on the fracture resistance of FDM printed materials. Proc SPIE 2017:1–9. https://doi.org/10.1117/12.2260105.
[29] Aliheidari N, Christ J, Tripuraneni R, Nadimpalli S, Ameli A. Interlayer adhesion and fracture resistance of polymers printed through melt extrusion additive manufacturing process. Mater Des 2018;156:351–61. https://doi.org/10.1016/j.matdes.2018.07.001.
[30] Park S, Watanabe N, Rosen DW. Estimating failure of material extrusion truss structures based on deposition modeling and a cohesive zone model. Mater Des 2018;147:122–33. https://doi.org/10.1016/j.matdes.2018.03.034.
[31] Young D, Wetmore N, Czabaj M. Interlayer fracture toughness of additively manufactured unreinforced and carbon-fiber-reinforced acrylonitrile butadiene styrene. Addit Manuf 2018;22:883–90. https://doi.org/10.1016/j.addma.2018.02.010.
[32] Khudiakova A, Arbeiter F, Spoerk M, Wolfahrt M, Godec D, Pinter G. Inter-layer bonding characterisation between materials with different degrees of stiffness processed by fused filament fabrication. Addit Manuf 2019;28:184–93. https://doi.org/10.1016/j.addma.2019.05.006.
[33] Spoerk M, Arbeiter F, Cajner H, Sapkota J, Holzer C. Parametric optimization of intra- and inter-layer strengths in parts produced by extrusion-based additive manufacturing of poly(lactic acid). J Appl Polym Sci 2017;134(41):45401. https://doi.org/10.1002/app.45401.
[34] Fonseca JV, Ferreira IA, de Moura MFSF, Machado M, Alves JL. Study of the interlaminar fracture under mode I loading on 3D printed parts. Compos Struct 2019;214:316–24.
[35] García-Guzmán L, Távara L, Reinoso J, Justo J, París F. Fracture resistance of 3D printed adhesively bonded DCB composite specimens using structured interfaces: Experimental and theoretical study. Compos Struct 2018;188:173–84. https://doi.org/10.1016/j.compstruct.2017.12.055.
[36] Ameri B, Taheri-Behrooz F, Aliha MRM. Mixed-mode tensile/shear fracture of the additively manufactured components under dynamic and static loads. Eng Fract Mech 2022;260:108185. https://doi.org/10.1016/j.engfracmech.2021.108185.
[37] Rezaeian P, Ayatollahi MR, Nabavi-Kivi A, Mohammad Javad Razavi S. Effect of printing speed on tensile and fracture behavior of ABS specimens produced by fused deposition modeling. Eng Fract Mech 2022;266:108393. https://doi.org/10.1016/j.engfracmech.2022.108393.
[38] Ayatollahi MR, Nabavi-Kivi A, Bahrami B, Yazid Yahya M, Khosravani MR. The influence of in-plane raster angle on tensile and fracture strengths of 3D-printed PLA specimens. Eng Fract Mech 2020;237:107225. https://doi.org/10.1016/j.engfracmech.2020.107225.
[39] Vu I, Bass L, Meisel N, Bruce O, Williams CB, Dillard DA. Characterization of Mutli-Material Interfaces in PolyJet Additive Manufacturing. Solid Free Fabr Symp 2014:959–82.
[40] Vu IQ, Bass LB, Williams CB, Dillard DA. Characterizing the effect of print orientation on interface integrity of multi-material jetting additive manufacturing. Addit Manuf 2018;22:447–61. https://doi.org/10.1016/j.addma.2018.05.036.
[41] Morano C, Bruno L, Pagnotta L, Alfano M. Analysis of crack trapping in 3D printed bio-inspired structural interfaces. Procedia Struct Integr 2018;12:561–6. https://doi.org/10.1016/j.prostr.2018.11.063.
[42] Alfano M, Morano C, Bruno L, Muzzupappa M, Pagnotta L. Analysis of debonding in bio-inspired interfaces obtained by additive manufacturing. Procedia Struct Integr 2018;8:604–9. https://doi.org/10.1016/j.prostr.2017.12.059.
[43] Cano AJ, Salazar A, Rodríguez J. Effect of temperature on the fracture behavior of polyamide 12 and glass-filled polyamide 12 processed by selective laser sintering. Eng Fract Mech 2018;203:66–80. https://doi.org/10.1016/j.engfracmech.2018.07.035.
[44] Brugo T, Palazzetti R, Ciric-Kostic S, Yan XT, Minak G, Zucchelli A. Fracture mechanics of laser sintered cracked polyamide for a new method to induce cracks by additive manufacturing. Polym Test 2016;50:301–8. https://doi.org/10.1016/j.polymertesting.2016.01.024.
[45] Hitt DJ, Haworth B, Hopkinson N. Fracture mechanics approach to compare laser sintered parts and injection mouldings of nylon-12. J Eng Manuf Part B 2011;225(9):1663–72. https://doi.org/10.1177/0954405411402141.
[46] Stoia DI, Marsavina L, Linul E. Mode I fracture toughness of polyamide and alumide samples obtained by selective laser sintering additive process. Polymers 2020;12(3):640. https://doi.org/10.3390/polym12030640.
[47] Linul E, Marsavina L, Stoia DI. Mode I and II fracture toughness investigation of Laser-Sintered Polyamide. Theor Appl Fract Mech 2020;106:102497. https://doi.org/10.1016/j.tafmec.2020.102497.
[48] Marşavina L, Stoia DI, Linul E. Fracture toughness in additive manufacturing by selective laser sintering: an overview. Mater Des Process Commun 2021;3:1–7. https://doi.org/10.1002/mdp2.254.
[49] Schneider J, Kumar S. Multiscale characterization and constitutive parameters identification of polyamide (PA12) processed via selective laser sintering. Polym Test 2020;86:106357. https://doi.org/10.1016/j.polymertesting.2020.106357.
[50] Zanetto J-E, Plummer CJG, Bourban P-E, Månson J-A- E. Fusion Bonding of Polyamide 12. Polym Eng Sci 2001;41(5):890–7.
[51] Reis JP, de Moura MFSF, Moreira RDF, Silva FGA. Pure mode I and II interlaminar fracture characterization of carbon-fibre reinforced polyamide composite. Compos Part B 2019;169:126–32. https://doi.org/10.1016/j.compositesb.2019.03.069.
[52] EOS GmbH. PA2200 Balance 1.0 Technical Data Sheet; 2018.
[53] Fonseca J, Ferreira IA, de Moura MFSF, Machado M, Alves JL. Study of the interlaminar fracture under mode I loading on FFF printed parts. Compos Struct 2019;214:316–24. https://doi.org/10.1016/j.compstruct.2019.02.005.
[54] Silva FGA, de Moura MFSF, Dourado N, Xavier J, Pereira FAM, Morais JJL, et al. Fracture characterization of human cortical bone under mode II loading using the end-notched flexure test. J Int Fed Med Biol Eng 2017;55(8):1249–60. https://doi.org/10.1007/s11517-016-1586-6.
[55] Pilipović A, Brajlih T, Drstvenšek I. Influence of processing parameters on tensile properties of SLS polymer product. Polymers 2018;10(11):1208. https://doi.org/10.3390/polym10111208.
[56] Stoia DI, Marşavina L, Linul E. Correlations between process parameters and outcome properties of laser-sintered polyamide. Polymers 2019;11(11):1850. https://doi.org/10.3390/polym11111850.
[57] Stoia DI, Marsavina L, Linul E. Mode I critical energy release rate of additively manufactured polyamide samples. Theor Appl Fract Mech 2021;114:102968. https://doi.org/10.1016/j.tafmec.2021.102968.